



## OPEN ACCESS

## EDITED BY

Bo-Tao Huang,  
Zhejiang University, China

## REVIEWED BY

Encarnacion Ruiz-Agudo,  
University of Granada, Spain  
Syahrul Fithry Senin,  
Cawangan Pulau Pinang, Malaysia

## \*CORRESPONDENCE

Arne Peys,  
✉ arne.peys@vito.be

RECEIVED 03 February 2025

ACCEPTED 28 April 2025

PUBLISHED 13 May 2025

## CITATION

Peys A, Pires Martins N, Prado Araujo F and  
Nielsen P (2025) Akermanitic clinker unlocks  
the potential of Mg-silicates for carbonation  
cured construction materials.

*Front. Mater.* 12:1570367.

doi: 10.3389/fmats.2025.1570367

## COPYRIGHT

© 2025 Peys, Pires Martins, Prado Araujo and  
Nielsen. This is an open-access article  
distributed under the terms of the [Creative  
Commons Attribution License \(CC BY\)](#). The  
use, distribution or reproduction in other  
forums is permitted, provided the original  
author(s) and the copyright owner(s) are  
credited and that the original publication in  
this journal is cited, in accordance with  
accepted academic practice. No use,  
distribution or reproduction is permitted  
which does not comply with these terms.

# Akermanitic clinker unlocks the potential of Mg-silicates for carbonation cured construction materials

Arne Peys<sup>1\*</sup>, Natalia Pires Martins<sup>1</sup>, Fernando Prado Araujo<sup>2</sup> and Peter Nielsen<sup>1</sup>

<sup>1</sup>Materials and Chemistry, Vlaamse Instelling voor Technologisch Onderzoek (VITO), Mol, Belgium,

<sup>2</sup>Department of Earth and Environmental Sciences, KU Leuven, Leuven, Belgium

The global CO<sub>2</sub> storage potential of Mg-silicate minerals is renowned. The valorization of residues containing these minerals via *ex situ* carbonation therefore seems an obvious pathway, however, significant levels of CO<sub>2</sub> uptake have only been obtained for a limited range of minerals (e.g., olivines), using extreme reaction conditions or strong chemicals. This paper shows that the carbonatability of Mg-silicate resources can be engineered using a clinkering process to produce akermanite (Ca<sub>2</sub>MgSi<sub>2</sub>O<sub>7</sub> or C<sub>2</sub>MS<sub>2</sub>), by heating a raw meal of Mg-silicates with 25–45 wt% of CaCO<sub>3</sub> to 1,200°C–1,350°C. Akermanitic clinkers with optimized raw meal obtained 40–70 wt% crystalline akermanite and 70–85 wt% total akermanite (including potential nanocrystalline akermanite from the XRD amorphous part). Carbonation of pressed cylinders at 10 bar, 60°C, 100% CO<sub>2</sub> and >90% RH provided 60–80 MPa compressive strength and a CO<sub>2</sub> uptake of about 100 kg/t, revealing the new akermanitic clinker as potential binder for construction materials.

## KEYWORDS

ferronickel slags, silicate mine tailings, mineral carbonation, carbonation curing, carbonatable clinker, akermanite

## 1 Introduction

Industries depend on carbon capture to ensure a complete transition to carbon neutrality (CEMBUREAU, 2016; Eurofer, 2019). Mineral carbonation offers a permanent storage of CO<sub>2</sub> through the chemical reaction with Ca or Mg-containing minerals into carbonates (Woodall et al., 2019; Snæbjörnsdóttir et al., 2020; Yadav and Mehra, 2021). This can be done *in situ*—by pumping CO<sub>2</sub> into a geological storage which is composed of carbonatable minerals—or *ex situ*—by enforcing the carbonation reaction in shorter time-frames in a reactor (Sanna et al., 2014). Although the latter has been previously considered costly (Veetil and Hitch, 2020), more recent developments show that economic processes can be obtained when suitable precursors are selected (Yadav and Mehra, 2021) or when simultaneously construction materials are produced (Woodall et al., 2019). Especially in industrial symbiosis, when process emissions are directly used for the carbonation of an alkaline residue (Nielsen et al., 2020), the economic and ecological incentives are massive.

One of the main challenges for maximizing the global impact is the search for suitable precursors, which can deliver economic carbonation by directly using process emissions (Yadav and Mehra, 2021). To enable that, near-ambient pressures (1–2 bar) and low

CO<sub>2</sub> concentrations (5%–20%) have to be applied. High-strength construction materials (30–60 MPa compressive strength) have currently only been made in these conditions when calcium silicates are present in sufficient quantities in the precursor, which is for instance observed for steel slags (Nielsen et al., 2020). From the volume perspective, the effective carbonation of magnesium silicates would substantially increase the absolute global CO<sub>2</sub> uptake. Most literature reports pressures of 65–135 bar at 150°C–185°C for achieving substantial carbonation without delivering useable end-products (Hamdallah Béarat et al., 2006; Li et al., 2019; Stephen Stokreef et al., 2022), endangering the economic feasibility of this process. Research on adapting the processing conditions (e.g., high-intensity stirring) or the use of admixtures (e.g., NaHCO<sub>3</sub>) has not been able to lower the pressure and temperature to industry-relevant conditions (Chizmeshya et al., 2007; Fei Wang et al., 2019). The production of Mg-oxide from Mg-silicates (MOMS) is increasingly researched, due to the possibility of carbonating MgO at atmospheric pressures (Gartner and Sui, 2018; Bernard et al., 2023). In this process, the Mg-silicate (often olivine) is dissolved in an acid or alkaline solution after which drying and calcination results in MgO formation. The literature is not clear on the recoverability of the chemicals needed for the MOMS process and the consumption of chemicals might therefore be a major issue of the concept.

A route to provide sufficient raw materials for *ex situ* mineral carbonation close to the traditional habits of the cement industry is the production of clinker (Gartner and Sui, 2018; Liu et al., 2023). The clinkers produced for carbonation found in literature are different from Portland clinker with respect to their Ca/Si ratio, but they still are mostly composed of calcium silicates with a minor content of iron and aluminium-containing phases to control the burnability. The technological framework for the clinkering process is thus exactly the same and using the same equipment and factories should be possible. Due to the lower Ca/Si ratio, the target phase assemblage is a mixture of dicalcium silicates (C<sub>2</sub>S), rankinite (C<sub>3</sub>S<sub>2</sub>), and/or wollastonite (CS), which are readily carbonatable at pressures <10 bar and can be produced at 1,250°C–1,400°C depending on the exact target quantitative phase assemblage (Hou et al., 2020; Lv et al., 2023). Next to the calcium silicates, phases from the melilite family (akermanite Ca<sub>2</sub>MgSi<sub>2</sub>O<sub>7</sub> and gehlenite Ca<sub>2</sub>Al<sub>2</sub>SiO<sub>7</sub>) can be present if the raw meal contains Mg or Al (Wang et al., 2024). Despite the low reactivity of melilite in steel slags (Librandi et al., 2019) and calcium silicate carbonation clinkers (Wang et al., 2024), recent findings show excellent properties of carbonated compacts when deliberately modifying ferronickel slags using CaCO<sub>3</sub> additions to contain akermanite (Peys et al., 2025). The modified slags still contained a substantial amount of Mg and Ca locked in unreactive phases, suggesting that the full potential was not reached. A clinkering process that maximizes the akermanite content might overcome this.

The present paper investigates the potential of clinker with a maximized akermanite content for mineral carbonation. Raw meals are composed of CaCO<sub>3</sub> and 3 Mg-silicate sources: a ferronickel slag, a silicate mine tailing, and a commercial Mg-silicate. Clinkers are produced with varying dosages of CaCO<sub>3</sub> to maximize the akermanite content. These dosages and the clinkering temperature are pre-designed using thermodynamic simulations and optimized experimentally. A variety of clinker compositions

is produced to maximize akermanite content, while scanning the possible secondary phases and phase assemblages to propose calculations for estimating the ideal raw meal formulation. The clinker with maximum akermanite content for each Mg-silicate source is screened for strength and CO<sub>2</sub> uptake after carbonation at 10 bar, 60°C, 100% CO<sub>2</sub>. The strongest sample is selected to study the carbonate phase assemblage and microstructure. Using this experimental strategy, this paper tries to provide the first assessment of the potential of carbonatable akermanitic clinkers in view of producing carbon neutral construction materials, as well as provide a first insight into the processing and characteristics of this new binder system.

## 2 Materials and methods

### 2.1 Materials

Three sources of Mg-silicates are investigated to enable obtaining general insights into the system. Ferronickel slag (FS), slowly cooled after production of ferronickel from laterite, silicate tailings (ST) from the mining of sulfidic ores for Ni, Cu, and Co production, and a commercially available Mg-silicate sold as olivine sand (OS) were obtained. The chemical composition was measured using X-ray fluorescence (XRF), shown in Table 1.

### 2.2 Thermodynamic simulations and clinker synthesis

The akermanitic clinkers are prepared by blending the magnesium silicates with CaCO<sub>3</sub>. Thermodynamic simulations were carried out to pre-optimize the raw meals and process temperature. The Equilib module of FactSage 8.2 (Bale et al., 2016) was used with the FactPS and FT Oxid databases. The equilibrium phase composition of blends of Mg-silicates and CaCO<sub>3</sub> was simulated as a function of temperature using steps of 10 wt% CaCO<sub>3</sub>. The steps are further refined to 5 wt% CaCO<sub>3</sub> for akermanite-forming compositions. No phases were excluded from the simulations and when alternative structures are proposed, the first option was selected. Simulations were carried out at 800°C–1,400°C and 1 bar using a fixed pO<sub>2</sub> of 10<sup>-1</sup> (=10% O<sub>2</sub>, which is common in kilns).

The raw meals were blended as dry powders and 8 wt% moisture was added before shaping into cylinders of 23 mm diameter and 20–22 mm height using 150 kgf/cm<sup>2</sup> in a hydraulic press. Formulations with varying CaCO<sub>3</sub> content were studied for all Mg-silicate resources, while for the ferronickel slag also formulations with additional SiO<sub>2</sub> were investigated (Table 2). Clinkering of the cylinders was done on a Pt tray for 30 min at 1300°C (unless another temperature is explicitly mentioned) using a rate of 3°C/min. Thermodynamic modelling indicated that for all formulations 1300 °C was 50°C–100°C below the temperature where collapse of the pellet would be expected (~50 wt% melt according to (Peys et al., 2021)). For the clinkers based on silicate tailings, the clinkering temperature was reduced to 1,200°C due to the observation of melting in experiments at 1300 °C and collapse of the pellet, which caused issues in recovering the pure material for characterization. The effect of varying the clinkering temperature 1,200°C–1,350°C

TABLE 1 Chemical composition of the Mg-silicate sources (XRF, relative error 5%–10%).

	SiO <sub>2</sub>	MgO	FeO	CaO	Al <sub>2</sub> O <sub>3</sub>	Others	LOI
FS	50.5	25.1	15.4	2.7	5.1	1.2	0.0
ST	45.4	22.2	10.5	13.7	4.2	1.9	2.1
OS	40.2	38.2	7.3	1.9	1.7	0.7	10.0

TABLE 2 Overview of clinker formulations.

Sample label	Magnesium silicate source	CaCO <sub>3</sub> dosage (wt% of raw meal)
FS_40	Ferronickel slag	40
FS_45	Ferronickel slag	45
FS_50	Ferronickel slag	50
FS_55	Ferronickel slag	55
FS_45Cc_5S	Ferronickel slag	45 (+5 wt% SiO <sub>2</sub> )
FS_50Cc_5S	Ferronickel slag	50 (+5 wt% SiO <sub>2</sub> )
FS_50Cc_10S	Ferronickel slag	50 (+10 wt% SiO <sub>2</sub> )
ST_20	Silicate mine tailings	20
ST_25	Silicate mine tailings	25
ST_30	Silicate mine tailings	30
ST_35	Silicate mine tailings	35
OS_15	Commercial magnesium silicate olivine sand	15
OS_20	Commercial magnesium silicate olivine sand	20
OS_25	Commercial magnesium silicate olivine sand	25
OS_30	Commercial magnesium silicate olivine sand	30

was afterwards investigated for the ferronickel slag-based clinkers. Due to the potential presence of asbestiform amphiboles in the tailings, the freedom for experimentation with those formulations was limited and a lab certified for asbestos detection provided confirmation of the absence of asbestos in the clinkers before proceeding to milling. In other words, the clinkering process can be seen as a process for asbestos destruction. Crushing in a disc mill and milling in a planetary ball mill was carried out until the clinkers reached a d50 of 8–12 μm. The latter was measured using laser diffraction on a Horiba. Prior to laser diffraction, deagglomeration using ultrasound was carried out for 2 min. The refractive index used in the calculations of the particle size was 1.7 + 0.1i.

## 2.3 Clinker characterization

The chemical composition was obtained from X-ray fluorescence (XRF) on powder samples. X-ray diffraction (XRD) was carried out to reveal the phase composition. The samples were milled <63 μm and mounted onto the sample holder using the back-loading method. The samples were in the lab sealed in ziplock bags, but not stored for long before analysis. The samples were measured at 40 kV and 45 mA on a PANalytical Empyrean with a Co source using a step size of 0.0131° 2θ and counting time of 0.02 s/step. The identification of phases was carried out in HighScore X'Pert Plus using phases from the PDF-4 database. Matching phases were selected after assessing their quality and relevance. An overview of selected phases indicating their database number is provided in the [Supplementary Material](#). Rietveld refinement in HighScore X'Pert Plus quantified the phase composition and was used for checking the completeness of the phase identification. The amorphous content was quantified using an external rutile standard, which was measured under the same conditions at the samples a maximum of 10 days before/after the sample measurements. More details about the analyses are described in the [Supplementary Material](#). The microstructure of the clinkers was investigated after crushing in the disc mill using scanning electron microscopy (SEM). The crushed material was embedded in epoxy resin and polished to study cross sections of the particles. Backscattered electron (BSE) images were taken on a FEI Nova NanoSEM 450 after coating with Pt/Pd alloy.

## 2.4 Carbonation procedure and analysis of carbonated material

The carbonation of the clinkers and raw magnesium silicates was carried out after pressing cylinders of 23 mm diameter and 20–23 mm height using a force of 150 kgf/cm<sup>2</sup>. The carbonation is carried out in a reactor for 16 h using 100% CO<sub>2</sub>, 60°C, and 10 barg. The carbonated cylinders were measured for compressive strength and total carbon (TC) content using a multi EA 4,000 analyzer. Thermogravimetric analysis (TGA) and differential thermogravimetric analysis (DTG) were carried out from room temperature to 1,000°C at 10°C/min using a nitrogen flow of 250 mL/min or CO<sub>2</sub> flow of 122 mL/min. The instrument used was a NETSCH–STA 449 F3 Jupiter coupled to a Mass spectrometer (MS) (NETSCH - QMS 403 D Aeolus).

An additional cylinder of 10 mm height was produced from the clinker sample FS\_45Cc and carbonated in the conditions mentioned above for SEM and Raman analysis. The sample was cut

and polished after carbonation to study the cross section (coating and equipment was the same as for the clinkers). Raman spectra were obtained using a Horiba Jobin-Yvon LabRAM HR Evolution spectrometer with a 532 nm wavelength laser (Nd:YAG, Oxxius,  $\times 100\text{mW}$  power) and  $\times 100$  objective (Olympus LMPLFLN, NA 0.8) coupled with an Olympus BX41 confocal microscope. Recording of the spectra was carried out using a spectral resolution of 150 grooves/mm grating, 10% laser power, 50  $\mu\text{m}$  confocal pinhole, and 15 s acquisition time with four repetitions.

## 3 Results and discussion

### 3.1 Composition of raw materials and optimal $\text{CaCO}_3$ dosing

The phase composition of the raw magnesium silicates provides a hint of what type of materials the akermanitic clinker production applies to. Fitted diffractograms are provided in the [Supplementary Material](#) and the Rietveld quantification is provided in [Table 3](#). The ferronickel slag is predominantly composed of pyroxene minerals, of which most are of the enstatite composition ( $\text{MgSiO}_3$ ), with a minor amount of diopside ( $\text{MgCaSi}_2\text{O}_6$ ). An olivine mineral is also present, closest in composition to forsterite ( $\text{Mg}_2\text{SiO}_4$ ), although also hosting a substantial amount of iron in solid solution. An amorphous phase was present in a quantity of approximately 26 wt%. The silicate tailings are rich in diopside pyroxene ( $\text{MgCaSi}_2\text{O}_6$ ) and have a large amount of amphibole, presumably of tremolite-actinolite composition ( $\text{Ca}_2(\text{Mg, Fe})_5\text{Si}_8\text{O}_{22}(\text{OH})_2$ ), which is asbestiform. Other phases are present in minor quantities. The commercial olivine sand mostly contains lizardite, forsterite, and hornblende amphibole. The amorphous content of the tailings and olivine sand was not quantified accurately due to precautions taken to avoid contamination of the lab with potentially asbestiform material.

The phase composition at thermodynamic equilibrium was simulated as a function of  $\text{CaCO}_3$  addition. [Figure 1](#) shows the phase composition at 1200°C. With increasing  $\text{CaCO}_3$  addition enstatite ( $\text{MgSiO}_3$ ) turns into diopside ( $\text{CaMgSi}_2\text{O}_6$ ), which later turns into akermanite ( $\text{Ca}_2\text{MgSi}_2\text{O}_7$ ), which turns into monticellite ( $\text{CaMgSiO}_4$ ) and merwinite ( $\text{Ca}_3\text{MgSi}_2\text{O}_8$ ). The maximal akermanite content is largely related to the pyroxene/amphibole content of the raw magnesium silicates. In the tailings and slags, enstatite and diopside gradually transform into akermanite with  $\text{CaCO}_3$  addition, while the forsterite content is not much affected apart from the dilution effect. In the olivine sand, however, the total content of pyroxenes and amphiboles is lower than 20 wt%. During clinkering of that material, lizardite and hornblende decompose and, in the presence of  $\text{CaCO}_3$ , form secondary forsterite, diopside, and akermanite. The lower Mg:Si ratio of the slags and tailings (0.3 and 0.5, respectively) compared to the commercial olivine sand (Mg:Si = 1.2) provides an improved chemical balance in the raw meals that enhances akermanite formation. In contrast with most technologies to carbonate magnesium silicates in the literature, olivine minerals are not desirable for akermanitic clinker, but rather silicate-rich sources are preferred to maximize the active content of the clinker. From the simulations, the probable optimal ranges of  $\text{CaCO}_3$  for

TABLE 3 Phase composition of the raw magnesium silicates.

Phase	FS	ST	OS
Forsterite ( $\text{Mg}_2\text{SiO}_4$ )	18	8	18
Enstatite ( $\text{MgSiO}_3$ )	50		5
Diopside ( $\text{CaMgSi}_2\text{O}_6$ )	6	36	
Magnetite ( $\text{Fe}_3\text{O}_4$ )		6	1
Quartz ( $\text{SiO}_2$ )			
Dolomite ( $\text{CaMg}(\text{CO}_3)_2$ )			2
Hornblende ( $(\text{Ca,Na})_2(\text{Mg,Fe,Al})_5(\text{Al,Si})_8\text{O}_{22}(\text{OH})_2$ )			13
Tremolite/Actinolite ( $\text{Ca}_2(\text{Mg, Fe})_5\text{Si}_8\text{O}_{22}(\text{OH})_2$ )		38	
Lizardite ( $\text{Mg}_3\text{Si}_2\text{O}_5(\text{OH})_4$ )		2	60
Clinocllore ( $(\text{Mg,Fe})_5\text{Al}(\text{Si}_3\text{Al})\text{O}_{10}(\text{OH})_8$ )		6	
Biotite ( $\text{K}(\text{Mg,Fe})_3\text{AlSi}_3\text{O}_{10}(\text{F,OH})_2$ )		2	
Albite ( $\text{NaAlSi}_3\text{O}_8$ )		5	
Amorphous/unidentified	26	-	-

experimental clinker synthesis can be derived: 35-50 wt% for FS, 20-35 wt% for ST, and 15-30 wt% for OS.

The clinkers are synthesized and the quantitative analysis of the XRD is shown in [Figure 2](#). A good quantitative match with the simulated phase composition in [Figure 1](#) is obtained in most cases. A deviation in the minor phases is observed as also wollastonite and merwinite are formed during clinkering experiments, and especially the combined existence of merwinite and diopside is not expected from the simulations. These phases are expected to contribute to the reactions in the carbonation process ([Librandi et al., 2019](#)), so might not be a barrier to overcome. However, the presence of these phases indicates that the clinker reactions were not completed (due to kinetic or physical boundaries), as when diopside is in contact with merwinite the formation of additional akermanite should occur from the thermodynamic perspective, as suggested in [Figure 1](#). In the clinkers from the tailings, there is a higher combined concentration of diopside and merwinite due to the lower clinkering temperature (1,200°C instead of 1,300°C). This was necessary due to the melt-down of the ST clinker samples at 1,300°C. A first step towards understanding the effect of temperature is provided for the FS\_45 sample in the next section. The optimization of the temperature of the clinkering process as well as a detailed study of the reaction kinetics of akermanite formation and enhancing the control of the clinker burnability has to be investigated thoroughly in future work.

The akermanite content of the clinkers as a function of  $\text{CaCO}_3$  addition matches between experiment and simulations. In the slags-based and tailings-based clinkers, the akermanite content varied in the 22-49 wt% range, while a maximum of 27 wt% akermanite formed in the olivine sand-based clinkers.

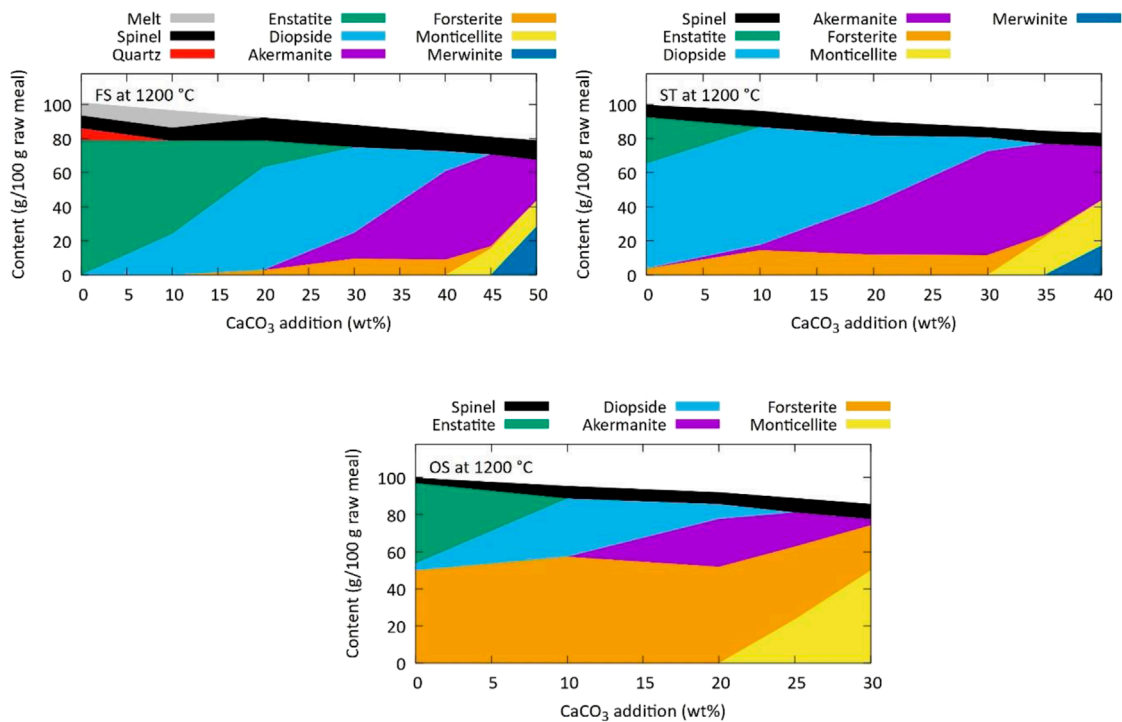


FIGURE 1 Simulated phase composition at thermodynamic equilibrium at 1200°C for the Mg-silicate sources as function of  $\text{CaCO}_3$  addition.

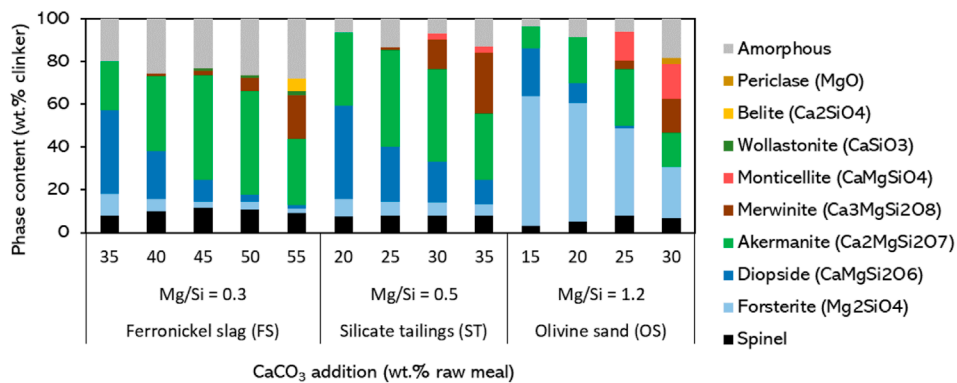
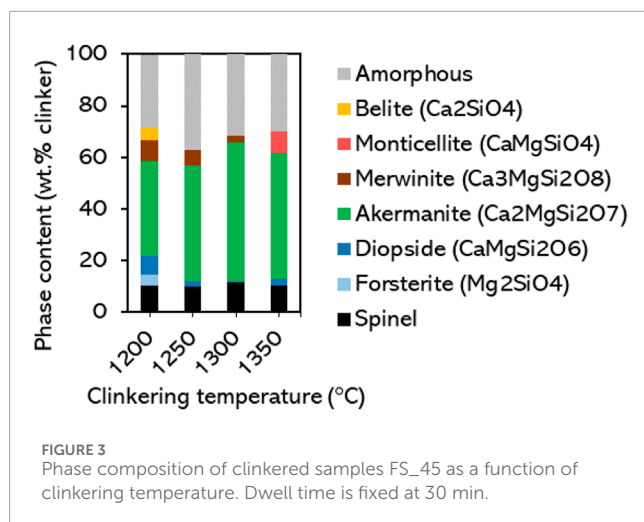


FIGURE 2 Measured phase composition of clinkered samples from the Mg-silicate sources as a function of  $\text{CaCO}_3$  addition.

This further confirms the suitability of pyroxene/amphibole-rich materials over olivine-rich raw materials for maximizing the akermanite content of clinkers. This provides an interesting distinction from most carbon sequestration technologies that researched Mg-silicates, which prefer olivine-rich raw materials (Bernard et al., 2023). The technology introduced in the present paper is thus rather complementary to direct carbonation technologies or MOMS, rather than a competition. Details on the determination of the phase compositions of the clinkers, as well as all refined XRD patterns, are shown in the [Supplementary Material](#).

### 3.2 Clinker phase assemblage as a function of temperature and with decreased Mg/Si

The clinkering process conditions are investigated in more detail using sample FS\_45, which showed a large akermanite content in [Figure 2](#). Clinkers were produced at different temperatures and varying the dwell times at maximum temperature. The influence of dwell time (15–60 min) is mostly seen at lower clinkering temperatures (1,200°C; see XRD patterns and Rietveld refinement results in [Supplementary Material](#)), where longer dwell times seem to favor the completeness of reactions. The effect of clinkering



temperature is shown in Figure 3. Compared to the clinker produced at 1300°C, lowering the clinkering temperature gradually lowers the akermanite content at the benefit of more diopside and merwinite. The content of akermanite decreases from 54 wt% at 1,300°C, to 45 wt% at 1,250°C and 37 wt% at 1,200°C. At 1,200°C, additional intermediates - belite and forsterite—are also detected, which further signals that the reactions are incomplete. Increasing the clinkering temperature to 1,350°C caused extensive melt formation, collapse of the pellet, and sticking to the crucible, although the material could still be recovered for XRD analysis. At that temperature, the content of akermanite decreases to 49 wt%. Figure 3 shows that in this case monticellite has formed and the phase composition is thus even closer to the thermodynamic simulations of Figure 1. The substantial melt formation observed at 1,350°C did not result in a significant increase of the amorphous content, the phases easily crystallized. The differences in phase composition between the replicated clinker samples FS\_45 in Figure 3 and the initial result in Figure 2 underline that the clinkering process conditions and its reaction kinetics must be investigated in more detail in future work to enhance the robustness of the process.

The substantial amount of XRD amorphous phase requires additional attention. A calculation from the already presented XRF and XRD data is tricky. Due to the solid solutions in the detected phases, some elements, in this case mostly Al, are not included in the crystalline composition even though it is probably present in the spinel, akermanite, and diopside. The calculation would thus unintentionally upconcentrate Al in the amorphous. SEM-EDS measurements are carried out on the sample FS\_45 clinkered at 1,300°C. Figure 4 shows BSE images and elemental maps of Si, Al, Fe, Mg, and Ca. The microstructure does not provide substantial differentiation between the phases, apart from the clear spinel grains and a matrix of akermanitic composition (during SEM operation also the minor content of merwinite could be traced, but this is not shown here). The XRD amorphous phase cannot be distinguished from the akermanite and has thus a very similar composition. This suggests that the XRD amorphous phase might rather be a nanocrystalline akermanite. The elemental maps also suggest the distribution of the major elements. Si and Ca are exclusively concentrated in the akermanite phase, while Fe is only present in

the spinel. There is also a significant concentration of Mg and Al in this spinel. The Mg is distributed equally between the spinel and akermanite, while the Al shows slightly higher concentrations in the spinel phase.

To further determine the boundaries of the system, formulations were made with the addition of SiO<sub>2</sub>. This is expected to completely deplete the forsterite from the system and indicate which Ca-silicate phase is stable with akermanite. The phase composition as a function of SiO<sub>2</sub> additions is provided in Figure 5 for the FS\_50 clinker. The SiO<sub>2</sub> additions effectively avoided the presence of forsterite, which causes an increased akermanite forming potential. However, it has to be noted that in some replicates (see Figure 3), forsterite was also not present without SiO<sub>2</sub> addition. This is related to the variability of the composition of the FS. The content of crystalline akermanite reached a maximum of 69 wt% with 10 wt% SiO<sub>2</sub> addition, in contrast to 46 wt% when no extra SiO<sub>2</sub> was added in the raw meal. When counting the amorphous content as nanocrystalline akermanite, the total akermanite content also slightly increased with SiO<sub>2</sub> addition: 75 wt% with 0 wt% SiO<sub>2</sub> and 85 wt. with 10 wt% SiO<sub>2</sub>. The highest addition of SiO<sub>2</sub> also results in the formation of pseudowollastonite during clinkering.

### 3.3 Phase relations and equations in akermanitic clinkers

With the determination of the range of phase compositions in akermanitic clinkers, the thermodynamic equilibrium discussed previously and shown on Figure 1 can be compared to the actual phases formed in experiments. The actual phases forming in akermanitic clinkers are corresponding in most cases with the thermodynamic equilibrium data at 1200 °C. The most important difference is the difficulty in forming monticellite in the experiments. Only at high clinkering temperatures when forming an amount of melt that results in a collapse of the clinker pellets, this phase was formed. It is thus expected that in a real clinkering process, this phase will not be formed and merwinite will be present instead. From the experimental phase compositions, the real phase relations are established and equations can be proposed to calculate the phase composition based on the raw meal chemical composition (similar to the Bogue equations (Bogue, 1929) in Portland clinkers). A ternary SiO<sub>2</sub>-CaO-MgO diagram highlighting the phases that co-exist with akermanite is provided in Figure 6.

The experimental ternary diagram shows four regions around the akermanite (C<sub>2</sub>MS<sub>2</sub>), which are indicated with the red numbers in Figure 6. Each region provides a combination of 3 phases, which next to akermanite (C<sub>2</sub>MS<sub>2</sub>) are forsterite (M<sub>2</sub>S), diopside (CMS<sub>2</sub>), pseudowollastonite (CS), and merwinite (C<sub>3</sub>MS<sub>2</sub>). The molar ratios between the phases in each region can be calculated from the molar ratios of Ca, Mg, and Si using the following matrix equations:

$$\begin{bmatrix} 2 & 1 & 0 & n_{C_2MS_2} & n_{Ca} \\ \text{region 1:1} & 1 & 2 \times n_{CMS_2} & = & n_{Mg} \\ 2 & 2 & 1 & n_{M_2S} & n_{Si} \end{bmatrix} \quad (1)$$

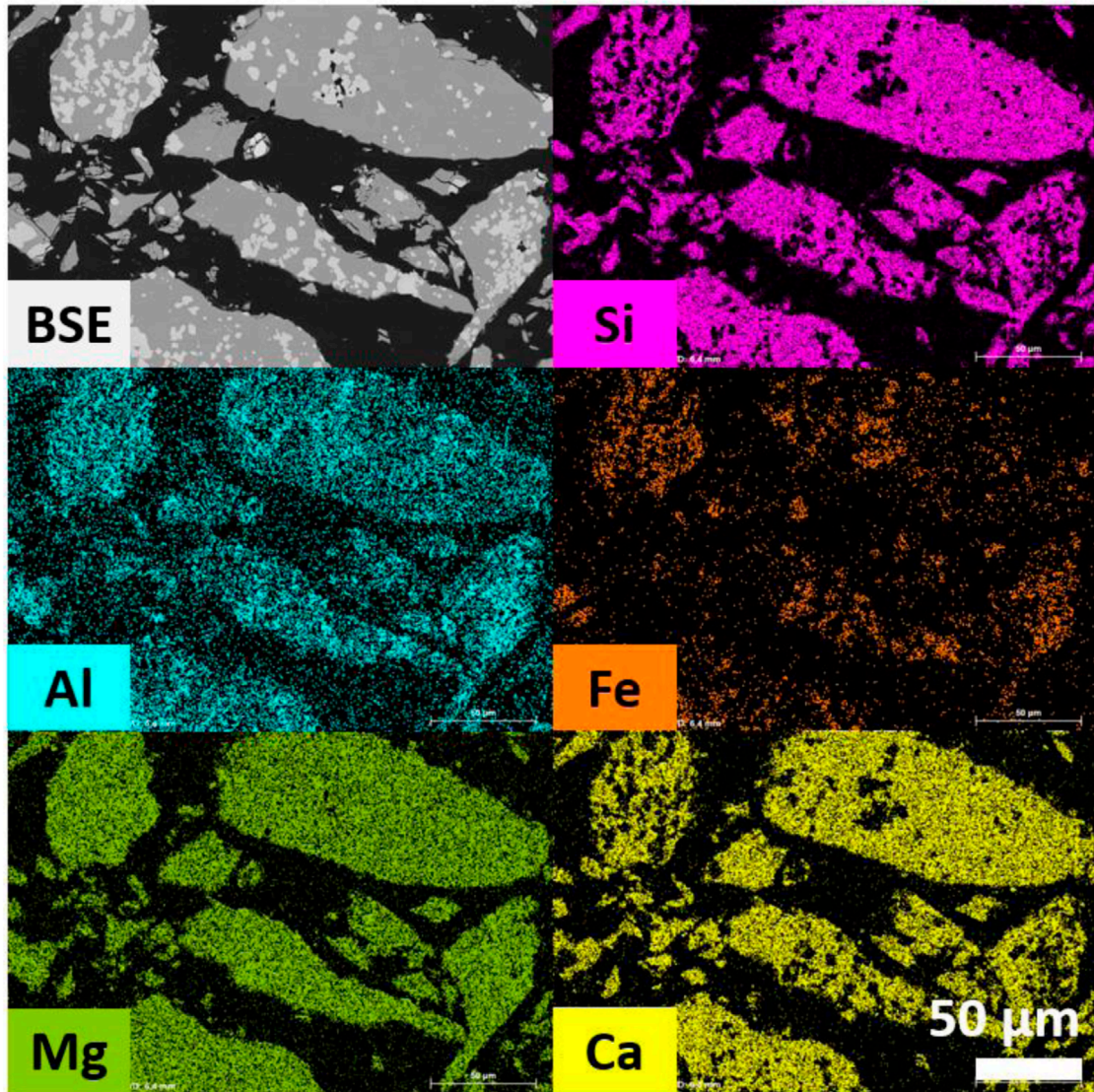


FIGURE 4 BSE image and elemental maps of polished sections of akermanitic clinker FS\_45.

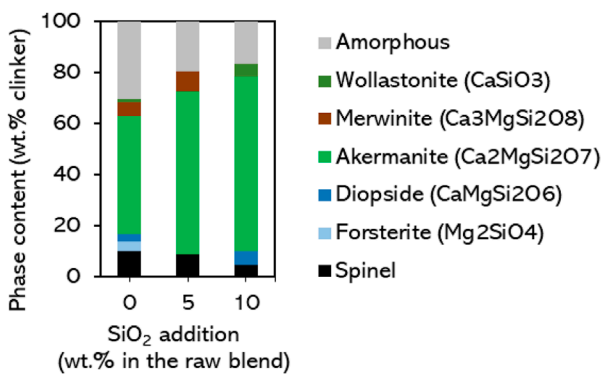


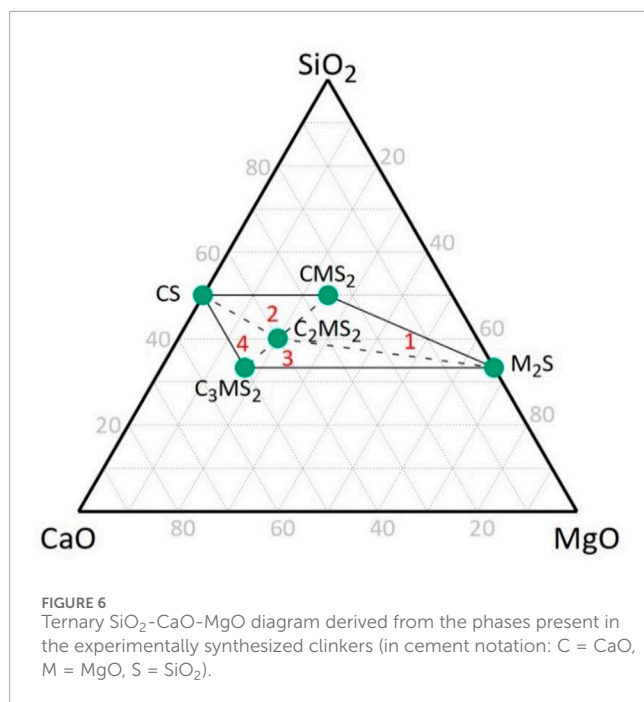
FIGURE 5 Phase composition of clinkered FS\_50 blends as a function of SiO<sub>2</sub> addition (S).

$$\begin{bmatrix} 2 & 1 & 1 & n_{C_2MS_2} & n_{Ca} \\ \text{region 2:1} & 1 & 0 \times n_{C_2MS_2} & = n_{Mg} & \\ 2 & 2 & 1 & n_{CS} & n_{Si} \end{bmatrix} \quad (2)$$

$$\begin{bmatrix} 2 & 0 & 3 & n_{C_2MS_2} & n_{Ca} \\ \text{region 3:1} & 2 & 1 \times n_{M_2S} & = n_{Mg} & \\ 2 & 1 & 2 & n_{C_3MS_2} & n_{Si} \end{bmatrix} \quad (3)$$

$$\begin{bmatrix} 2 & 3 & 1 & n_{C_2MS_2} & n_{Ca} \\ \text{region 4:1} & 1 & 0 \times n_{C_3MS_2} & = n_{Mg} & \\ 2 & 2 & 1 & n_{CS} & n_{Si} \end{bmatrix} \quad (4)$$

The molar ratios of Ca, Mg, and Si can be derived from the chemical composition of the raw meal and the phase composition can be calculated from the molar ratios of the phases obtained with



the matrix equations. Using a simplified assumption that Al and Fe will be present in spinel (or hercynite for compositions with a higher Al/Fe ratio), the complete clinker phase assemblage can be predicted. The [Supplementary Material](#) provides an Excel worksheet that provides this calculation. The phase compositions obtained from the raw meals investigated in this study are shown in [Figure 7](#), next to the results predicted using FactSage and to the phase compositions determined experimentally by XRD.

It was verified that the chemical composition of the raw meals containing the OS fell mostly outside the range of applicability of [Equations 1–4](#), despite the presence of akermanite in the corresponding clinkers. For that reason, the calculated phase composition of those clinkers is not shown in [Figure 7](#). The raw meals containing FS and ST, however, are aligned with the border between regions 2/4 and 1/3 (see ternary diagram in [Supplementary Figure S28](#)). Within those regions, [Equations 1–4](#) could be used, resulting in the predictions plotted in [Figure 7](#). The calculated phase compositions are largely in agreement with the phase compositions simulated using FactSage, except when it comes to the prediction of monticellite and merwinite. Given the limited formation of monticellite in the synthesized clinkers, the exclusion of this phase from the predictions using [Equations 1–4](#) was expected to result in more accurate predictions, which was generally confirmed for the spinel and forsterite. Yet, compared to the XRD results, the ratio between akermanite and merwinite is still not adequately predicted at higher CaCO<sub>3</sub> additions, resulting in over- or underestimation of akermanite. Moreover, similarly to FactSage, [Equations 1–4](#) do not predict the simultaneous presence of merwinite and diopside in the clinkers, which is often observed experimentally due to incomplete reaction of the raw meal. The difference of the XRD results with FactSage and Calculated phase compositions are further explained by inaccurate measurement of the chemical composition or phase composition; especially XRF, for which a relative error of 5%–10% was estimated, propagating a

substantial error into the calculations. Another effect which might contribute slightly is the appearance of solid solutions in the relevant phases of elements outside of the ternary, however, this is taken into account in the FactSage calculations and should therefore be seen as a difference between FactSage and Calculated phase compositions (unless these solid solutions are not accurately calculated in FactSage). Overall, the equations are sufficiently accurate for their intended purpose: they can be used to calculate what range of CaCO<sub>3</sub> additions might be suitable to start optimizing the clinker raw meal without the need for more complex thermodynamic calculations.

### 3.4 Strength and CO<sub>2</sub>-uptake of akermanitic clinkers

The clinker powders were shaped into cylinders and carbonated at 10 barg and 60°C using 100% CO<sub>2</sub> for 16 h. The strength and CO<sub>2</sub>-uptake after carbonation in [Figure 8](#) are compared between the raw magnesium silicates and their respective clinkers with the highest akermanite content. For the ferronickel slag and silicate tailings, the near-zero values are increased to compressive strength values that exceed most conventional construction materials when using the ST\_25 and FS\_45 clinker samples. More specifically, the strength of the carbonated ferronickel slag was 0.2 MPa and no significant CO<sub>2</sub>-uptake was measured, while the carbonated FS\_45 clinker achieved 77 Mpa and bound 100 kg CO<sub>2</sub> per ton of block. Figures similarly promising were obtained for the tailings. The underlying mechanism of the different ratio of strength and CO<sub>2</sub> uptake of the ST\_25 vs. FS\_45 has not been clarified at this stage, but this is a subject of future work. The lower values of strength and CO<sub>2</sub>-uptake reached by the OS-based carbonated clinker (OS\_25 treated) are consistent with the lower akermanite content in that clinker and suggest that the abundant forsterite ([Figure 1](#)) is not a major strength-giving phase at these conditions. Although forsterite can reach significant conversion rates at 185°C and P<sub>CO<sub>2</sub></sub> > 65 bar ([Li et al., 2019](#)), the results from this study suggest that this phase presents substantially lower reactivity towards CO<sub>2</sub> compared to akermanite when carbonating at 60°C and 10 barg.

### 3.5 Carbonation reaction mechanism and resultant microstructure

The carbonate phase assemblage was investigated using several complementary techniques. [Figure 9](#) shows the fitted diffractogram of carbonated FS\_45 with indications of clinker phases, Mg-calcite and aragonite contributions. This zoomed version making the main peaks of Mg-calcite and aragonite visible is provided here and a diffractogram of the full fitted range is provided in the [Supplementary Material](#). Mg-calcite and aragonite were also found in previous work when carbonating akermanite-containing modified ferronickel slag ([Peys et al., 2025](#)). Although XRD was not conclusive there, complementary Raman data confirmed the presence of both carbonates. In the present study with more pure akermanite clinkers, the XRD ([Figure 9](#)) is more clear and a quantification of the phase assemblage will be more accurate. The XRD pattern of the refined phase (in [Supplementary Material](#))

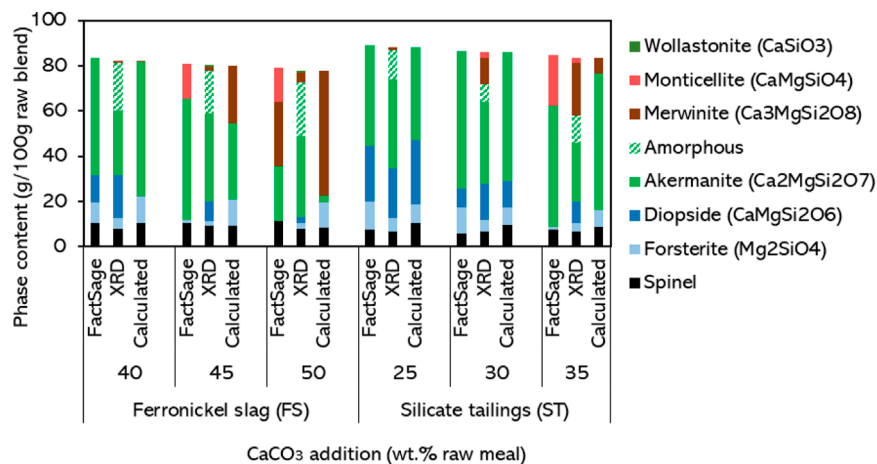


**FIGURE 7**  
Comparison of the phase composition of selected clinkers obtained experimentally by XRD, on FactSage simulations, and calculated using Equations 1–4. All results are rescaled to g per 100 g of raw meal.

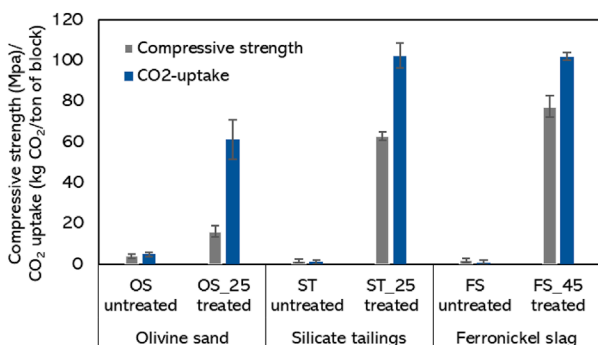


**FIGURE 8**  
Compressive strength and CO<sub>2</sub>-uptake of cylinders after carbonation at 10 barg and 60°C for 16 h of raw Mg-silicates and clinkers. The error bars represent the double of the standard deviation.

is clearly an intermediate between that of stoichiometric calcite and stoichiometric dolomite, indicating that it corresponds to a solid solution. The refined unit cell parameters,  $a = 4.86 \text{ \AA}$  and  $16.49 \text{ \AA}$ , were obtained after allowing a 5% variation from the initial values of the Mg-calcite structure PDF 04-026-3167. This refined unit cell is consistent with the incorporation of high concentrations of MgCO<sub>3</sub> in the structure, i.e., between 30 and 35 wt% (Floquet et al., 2020). An overview of the existing phases Ca, CaMg, and Mg-carbonate phases with a trigonal crystal system is provided in Figure 10 using the Co 2 $\theta$  angle of their 104 reflection to distinguish them, also indicating where the observed Mg-calcite was found. It was not possible to verify the exact composition using EDS due to the intermixing of fine Mg-calcite with other reaction products.

Raman spectroscopy of the carbonated samples in Figure 11 confirms that a carbonate binder has formed from the reaction of akermanite. The Raman spectrum of the akermanite phase in the carbonated sample clinker shows the occurrence of weak broad

bands at around 720 and 1080 cm<sup>-1</sup> that are not present in the reference spectrum. These bands may be related to the presence of CO<sub>3</sub> groups in the mineral structure (Urmos et al., 1991), although in this case it is most likely a minor reaction of the polished section with atmospheric CO<sub>2</sub>. The analysis of the binder shows a considerable increase in the intensity of these bands, while the intensity of akermanite bands decreases concomitantly. Regarding the identification of the carbonate phases, Raman spectroscopy suggests that the binder is not a pure phase with the number of bands and peak positions between aragonite and dolomite. This can thus confirm the XRD analysis on the presence of aragonite and a CaMg-carbonate phase and suggests that these carbonates are closely intermixed. Due to their mixing and the broad nature of the CaMg-carbonate it is not possible to obtain more information on the structure from Raman spectroscopy. Some broad bands (600–800 and 1,300–1,500 cm<sup>-1</sup>) that are not present in the reference spectra also indicate the presence of a disordered structure. The Raman shift of the bands indicates that this structure is similar to amorphous carbon (Ferrari and Robertson, 2000) and therefore the signal is likely a contamination.

Thermogravimetric analysis (TGA-MS data shown in Supplementary Material) carried out under a flow of N<sub>2</sub> indicates that the weight loss starting at around 370°C and ending at around 800°C can be attributed to the release of CO<sub>2</sub>. The total CO<sub>2</sub> released, derived from the mass loss between 370°C and 800°C, was 10.25 wt%, which is in good agreement with the 10.2 wt% CO<sub>2</sub> measured by TC analysis. Both estimates are higher than that based on the abundances of carbonate phases determined from the XRD analysis, i.e., 6.9 wt% CO<sub>2</sub>. This suggests the presence of XRD amorphous carbonate phases.

The initial mass release observed in the TGA between 370°C and 600°C, with a lack of clear DTG peaks is most likely (partly) related to amorphous carbonate phases, while the strong and sharp peak DTG between 650°C and 800°C can be attributed to the decomposition of crystalline carbonates (Figure 12). Note that aragonite is known to transform into calcite at ~450°C (Goto et al.,

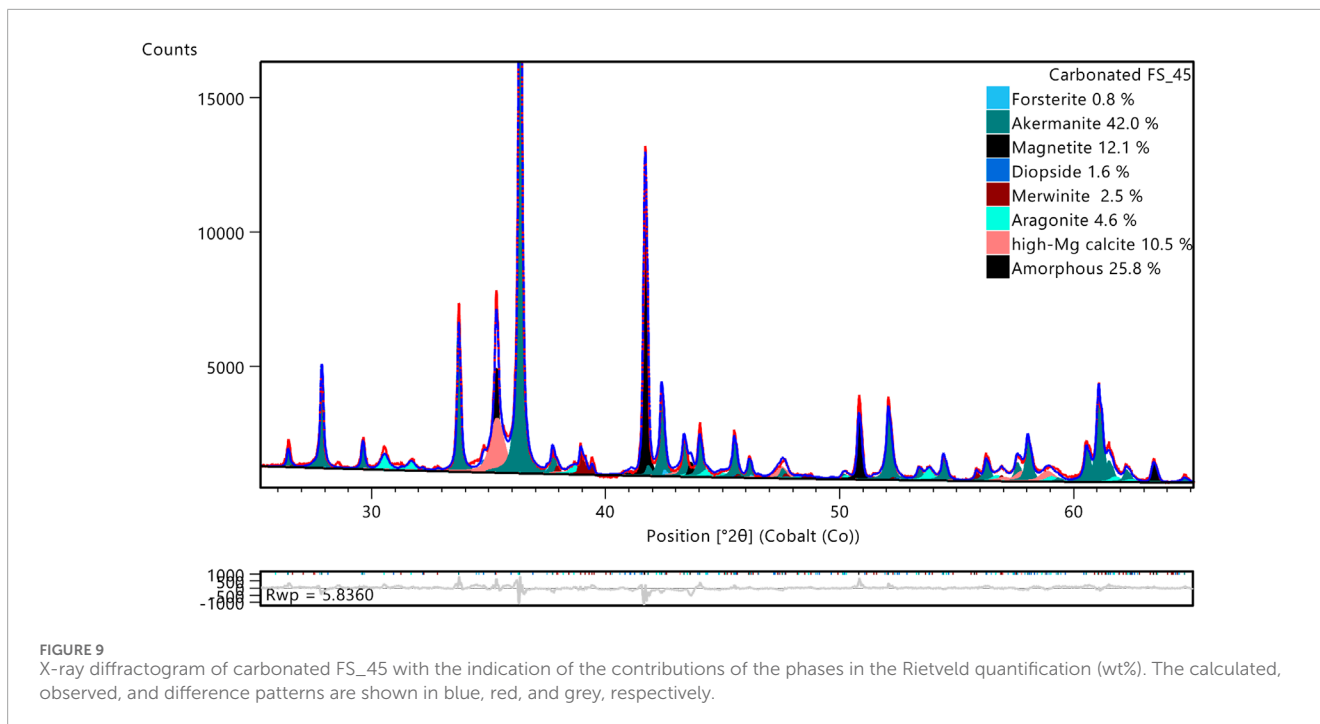


**FIGURE 9** X-ray diffractogram of carbonated FS\_45 with the indication of the contributions of the phases in the Rietveld quantification (wt%). The calculated, observed, and difference patterns are shown in blue, red, and grey, respectively.

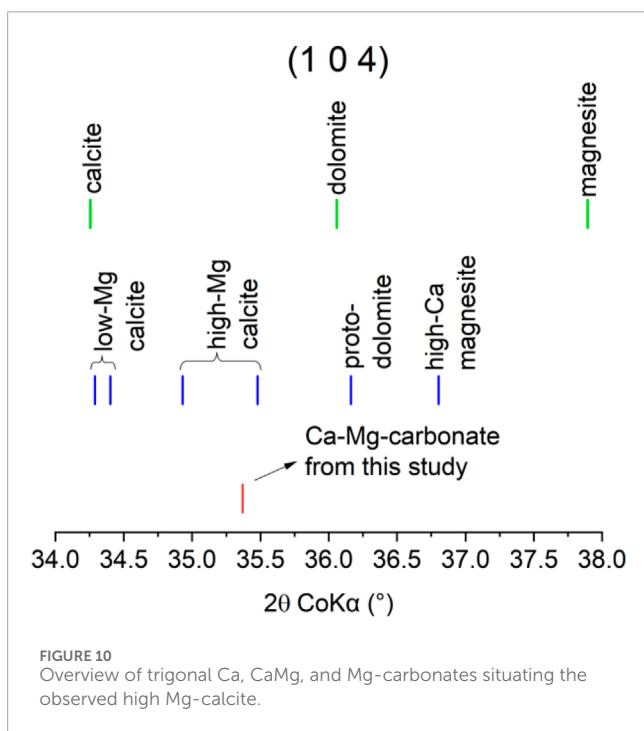
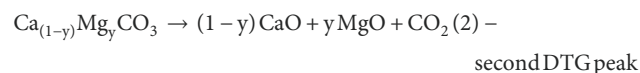
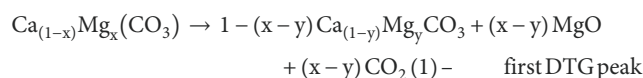


**FIGURE 10** Overview of trigonal Ca, CaMg, and Mg-carbonates situating the observed high Mg-calcite.

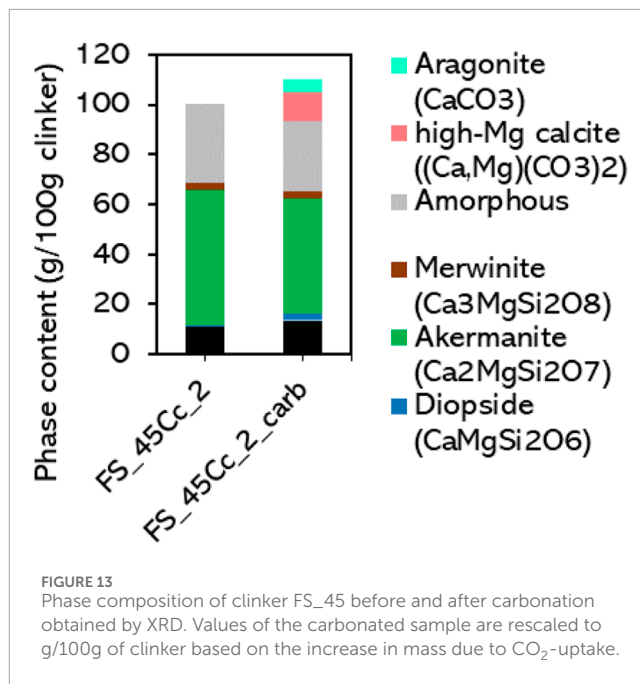
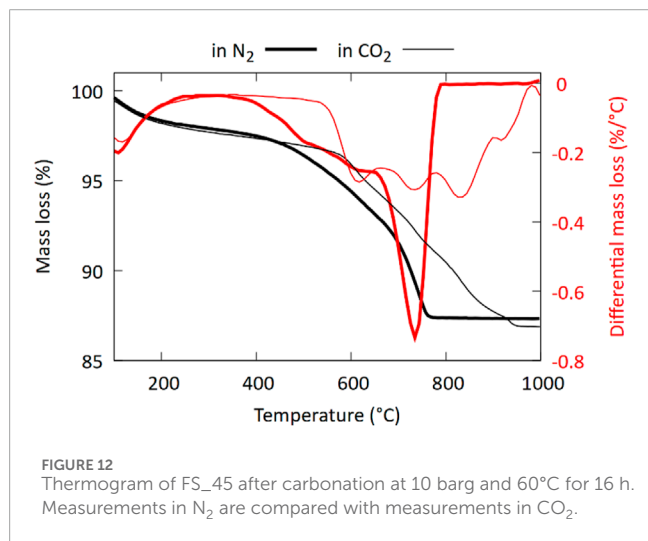
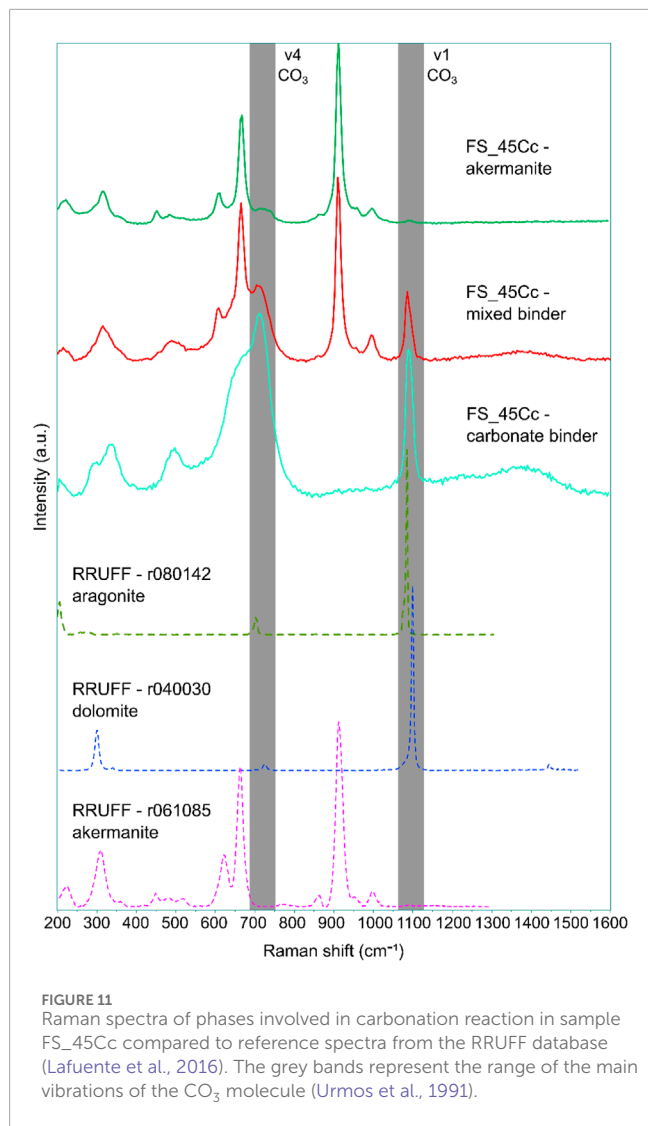
1995; Mu et al., 2018). This transformation is accompanied by a very small endothermic peak in the DTA curve (Goto et al., 1995). The decarbonation reaction, however, occurs at a temperature similar to that of calcite (Goto et al., 1995). Magnesian-calcites decompose in two steps. In the first step the high magnesian calcite decomposes into a low magnesian calcite (2.8–6 mol%) and MgO (Floquet et al., 2020), according to reaction (1), and in the second step the low

Mg-calcite decarbonates, according to reaction (2):



The starting temperature of this first decomposition reaction decreases as the Mg-content increases, from about 620°C for  $\text{Ca}_{0.76}\text{Mg}_{0.24}\text{CO}_3$  to 560°C for  $\text{Ca}_{0.6}\text{Mg}_{0.4}\text{CO}_3$  and 500°C for  $\text{Ca}_{0.50}\text{Mg}_{0.50}\text{CO}_3$  (Floquet et al., 2020). The second decomposition reaction occurs at similar temperatures as calcite, i.e., above 600°C (Goto et al., 1995). Patel et al. (Patel et al., 2024) observed a similar two step decarbonation process for amorphous CaMg-carbonates, with the amorphous Mg-carbonate (reaction 1) decomposing between 375 and 450°C–520°C (depending on the Mg content) and the amorphous Ca-carbonates (reaction 2) mainly decomposing between 600°C and 700°C ((Patel et al., 2024), Supplementary Figure S2).

When performing the TGA analysis under a flow of  $\text{CO}_2$ , we observe four different DTG peaks and a shift towards higher decomposition temperatures (Figure 12). For dolomite Valverde et al. (Valverde et al., 2015) showed that decarbonation of  $\text{MgCO}_3$  (reaction 1) is not fundamentally affected by the partial  $\text{CO}_2$  pressure, whereas the decomposition temperature of  $\text{CaCO}_3$  (reaction 2) is shifted towards higher temperatures as the  $\text{CO}_2$  partial pressure is increased (Otsuka, 1986; Valverde et al., 2015). Based on this the two DTG peaks observed at approximately 830°C and 920°C could be attributed to the decomposition of  $\text{CaCO}_3$  (either from aragonite or from a high-Mg calcite). The DTG peaks at lower temperature then likely represent the first



(MgCO<sub>3</sub>) decarbonation step from both amorphous and crystalline CaMg-carbonates. The higher initial decarbonation temperatures for the amorphous phases are likely linked to a crystallization process of the amorphous phases occurring in the CO<sub>2</sub> environment during heating.

The quantification of the different carbonate phases by TGA was not attempted because of the difficulty in assigning the DTG peaks to specific carbonate minerals and because of the overlapping of DTG peaks and the large spread in the results when using different deconvolution strategies.

After confirming the presence of aragonite and Mg-calcite, further elaboration on the XRD results of the carbonated sample can be done. To compare the Rietveld refinement results of clinkers before and after carbonation, the phase abundancies of the carbonated sample must be rescaled to a common basis (g per 100g of uncarbonated clinker). This was done considering that the mass change during carbonation corresponds to the gain in mass due to CO<sub>2</sub> uptake in the carbonated sample. The results are shown in Figure 13. In disagreement with a previous study where similar carbonation conditions were used (Smigelskyte et al., 2020), akermanite is the major reacting phase here. No other clinker phase showed extensive reaction in the investigated sample. Based on the XRD quantification of crystalline akermanite before and after carbonation, i.e., 54 wt% and 45 wt%, respectively, a reaction degree of 17% was reached. This estimate is, however, conservative, since the reaction of the XRD-amorphous fraction of akermanite is not taken into account. It must be noted that the reaction of the amorphous akermanite is consistent with the slightly lower amorphous content quantified in the carbonated sample. In that sample, the amorphous fraction not only corresponds to XRD-amorphous akermanite but also a contribution of a substantial fraction of amorphous carbonation products (carbonates and silica) is expected. The total reaction degree of akermanite (including XRD-amorphous akermanite) expected based on the CO<sub>2</sub> uptake

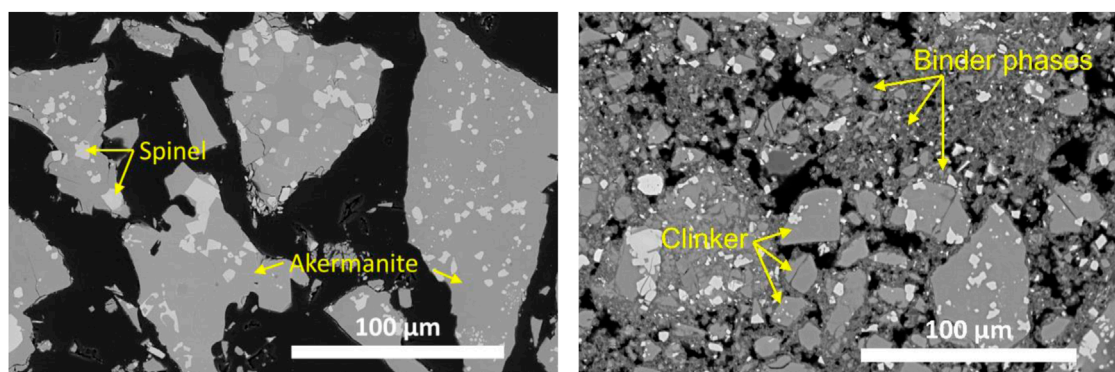


**FIGURE 14**  
BSE image of polished sections of the akermanitic clinker FS\_45 before (left) and after carbonation (right).

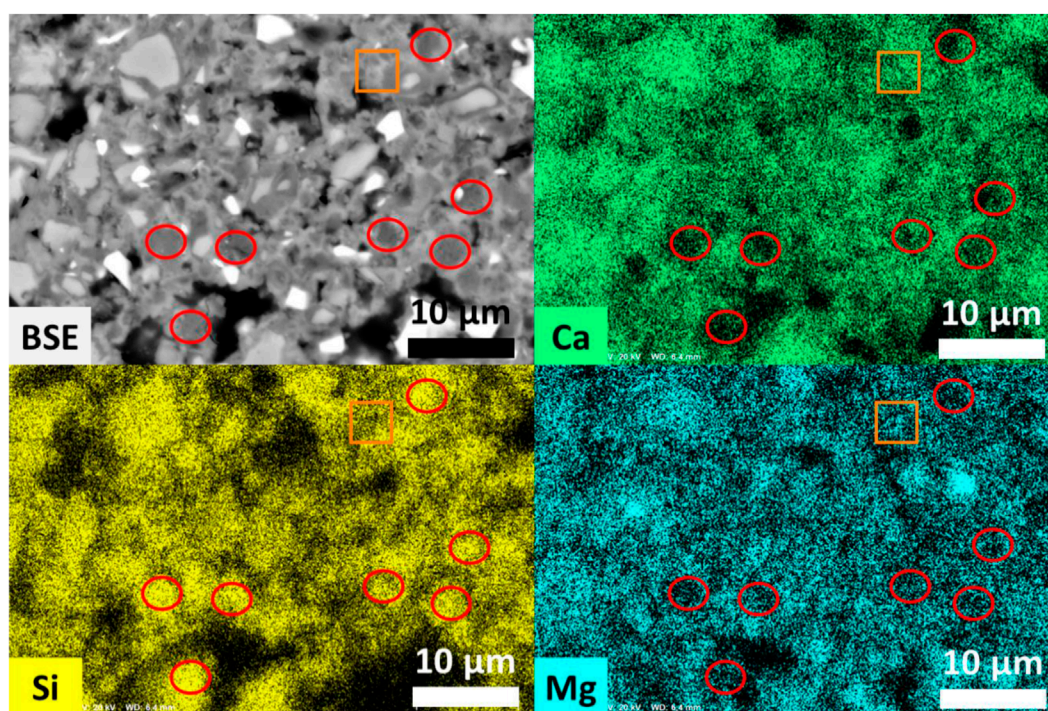


**FIGURE 15**  
BSE image and elemental maps of polished sections of carbonated akermanitic clinker FS\_45. Red circles indicate zones enriched in Si and poor in Ca, Mg - zones assigned to amorphous silica. The zone indicated in orange contains an example of carbonate product.

measured by TC analysis and TGA is in the order of magnitude of 40%, although future work should clarify the composition of the amorphous reaction products to provide a correct reaction formula to derive the reaction degree more accurately.

The microstructure of the akermanitic clinker and the carbonated FS\_45 sample are compared in the backscattered electron (BSE) images on polished sections in Figure 14. The clinker (left) looks homogeneous, showing the akermanite matrix in medium grey contrast and bright spots of spinel. The minor phases

diopside, forsterite, and merwinite are less easily distinguished from the akermanite matrix. After carbonation (right), partially reacted clinker particles are surrounded by carbonate binding phases and silica gel, forming the porous yet strong skeleton of the carbonated binder. A closer look at the carbonated binder is given in Figure 15. Elemental maps acquired at higher magnification show the existence of dark contrast zones enriched in Si and poor in Ca and Mg, corresponding to amorphous silica (red circles in Figure 15). Those zones are spread across the carbonated matrix and are also seen

as dark contrast rims surrounding akermanite particles. Structures in light grey contrast correspond to the carbonated products (orange square in Figure 14).

## 4 Conclusion

A process to enable the carbonation of Mg-silicate resources in 16 h at 10 barg in 100% CO<sub>2</sub> at 60 °C was developed. A range of Mg-silicate sources (ferronickel slag, silicate mine tailings, and commercial “olivine sand”) were used as raw materials for the production of akermanitic carbonatable clinkers. To maximize akermanite content, raw meals composed of 80–55 wt% of the Mg-silicate resource and 20–45 wt% CaCO<sub>3</sub>. Clinkering was carried out at 1,200°C–1350 °C. Especially the pyroxene and amphibole-rich ferronickel slag and silicate tailings provided a high akermanite content after clinkering with 45 wt% CaCO<sub>3</sub> and 25 wt% CaCO<sub>3</sub>, respectively. Asbestos was destroyed during clinkering. Olivine-rich resources, such as the olivine sand investigated here, did not result in high akermanite contents after clinkering with the addition of CaCO<sub>3</sub>. The crystalline akermanite content could be boosted up to 54 wt% in the ferronickel slag with 45 wt% of CaCO<sub>3</sub>, or even to 69 wt% when also adding SiO<sub>2</sub> to further lower the content of secondary phases such as forsterite. However, the amorphous fraction in the clinkers was shown to have the same composition as akermanite and should be seen as nanocrystalline akermanite. Total akermanite contents of the ferronickel slag-based clinkers were thus actually 75–85 wt%. An empirical ternary phase diagram was proposed from which the phase composition can be estimated based on the raw meal chemical composition, to facilitate efficient clinker formulations from new constituents.

Carbonation of pressed cylinders made from the high-akermanite clinkers at 10 bar in 100% CO<sub>2</sub> at 60°C resulted in a compressive strength of 60–80 MPa and CO<sub>2</sub>-uptake of 100 kg/t product. The akermanite, and especially nanocrystalline akermanite, had a substantial degree of carbonation and resulted in the formation of aragonite, high Mg-calcite, and amorphous silica. The other phases did not significantly contribute to the carbonation reaction. Overall, a new binder system was proposed with interesting properties, industry-relevant processes and conditions, and a substantially lower CO<sub>2</sub>-footprint compared to contemporary cementitious binders.

## Data availability statement

The original contributions presented in the study are included in the article/Supplementary Material, further inquiries can be directed to the corresponding author.

## Author contributions

AP: Conceptualization, Data curation, Formal Analysis, Funding acquisition, Investigation, Methodology, Project

administration, Supervision, Validation, Visualization, Writing – original draft, Writing – review and editing. NP: Data curation, Formal Analysis, Investigation, Methodology, Validation, Visualization, Writing – original draft, Writing – review and editing. FP: Data curation, Formal Analysis, Investigation, Methodology, Visualization, Writing – original draft, Writing – review and editing. PN: Formal Analysis, Investigation, Methodology, Supervision, Validation, Writing – original draft, Writing – review and editing.

## Funding

The author(s) declare that financial support was received for the research and/or publication of this article. The research leading to these results was conducted within the ENICON project, <https://enicon-horizon.eu/>, and received funding from the European Union’s Framework Programme for Research and Innovation Horizon Europe under Grant Agreement No. 101058124.

## Acknowledgments

The authors are thankful to Myrjam Mertens, Bo Peeraer, Sten Janssen, Kosar Hassannezhad, Nancy Dewit, Anne-Marie De Wilde, and Hilde Leppens for the experimental work.

## Conflict of interest

The authors declare that the research was conducted in the absence of any commercial or financial relationships that could be construed as a potential conflict of interest.

## Generative AI statement

The author(s) declare that no Generative AI was used in the creation of this manuscript.

## Publisher’s note

All claims expressed in this article are solely those of the authors and do not necessarily represent those of their affiliated organizations, or those of the publisher, the editors and the reviewers. Any product that may be evaluated in this article, or claim that may be made by its manufacturer, is not guaranteed or endorsed by the publisher.

## Supplementary material

The Supplementary Material for this article can be found online at: <https://www.frontiersin.org/articles/10.3389/fmats.2025.1570367/full#supplementary-material>

## References

- Bale, C. W., Bélsile, E., Chartrand, P., Decterov, S. A., Eriksson, G., Gheribi, A. E., et al. (2016). FactSage thermochemical software and databases, 2010–2016. *Calphad* 54, 35–53. doi:10.1016/j.calphad.2016.05.002
- Bernard, E., Nguyen, H., Kawashima, S., Lothenbach, B., Manzano, H., Provis, J., et al. (2023). MgO-based cements – current status and opportunities. *RILEM Tech. Lett.* 8, 65–78. doi:10.21809/rilemtechlett.2023.177
- Bogue, R. H. (1929). Calculation of the compounds in Portland cement. *Industrial and Eng. Chem. Anal. Ed.* 1 (4), 192–197. doi:10.1021/ac50068a006
- CEMBUREAU (2016). The role of cement in the 2050 low carbon economy. *Bruss. Eur. Cem. Assoc.*
- Chizmeshya, A. V. G., Kyle Squires, M. J. M., Carpenter, R. W., and Béarat, H. (2007). A novel approach to mineral carbonation: enhancing carbonation while avoiding mineral pretreatment process cost. United States: Arizona State Univ.
- Eurofer (2019). Low carbon roadmap: pathways to a CO<sub>2</sub>-neutral European steel industry.
- Fei Wang, D. D., Jarvis, M., Hitchins, T., and Hitchins, T. (2019). Kinetics and mechanism of mineral carbonation of olivine for CO<sub>2</sub> sequestration. *Miner. Eng.* 131, 185–197. doi:10.1016/j.mineng.2018.11.024
- Ferrari, A. C., and Robertson, J. (2000). Interpretation of Raman spectra of disordered and amorphous carbon. *Phys. Rev. B* 61 (20), 14095–14107. doi:10.1103/PhysRevB.61.14095
- Floquet, N., Vielzeuf, D., Heresanu, V., Laporte, D., and Perrin, J. (2020). Synchrotron high-resolution XRD and thermal expansion of synthetic Mg calcites. *Phys. Chem. Minerals* 47 (11), 48. doi:10.1007/s00269-020-01115-5
- Gartner, E., and Sui, T. (2018). Alternative cement clinkers. *Cem. Concr. Res.* 114, 27–39. doi:10.1016/j.cemconres.2017.02.002
- Goto, S., Suenaga, K., Kado, T., and Fukuhara, M. (1995). Calcium silicate carbonation products. *J. Am. Ceram. Soc.* 78 (11), 2867–2872. doi:10.1111/j.1151-2916.1995.tb09057.x
- Hamdallah Béarat, M. J. M., Chizmeshya, A. V. G., Gormley, D., Nunez, R., Carpenter, R. W., Squires, K., et al. (2006). Carbon sequestration via aqueous olivine mineral carbonation: role of passivating layer formation. *Environ. Sci. Technol.* 40 (15), 4802–4808. doi:10.1021/es052334o
- Hou, G., Chen, J., Lu, B., Chen, S., Cui, E., Naguib, H. M., et al. (2020). Composition design and pilot study of an advanced energy-saving and low-carbon rankinite clinker. *Cem. Concr. Res.* 127, 105926. doi:10.1016/j.cemconres.2019.105926
- Lafuente, B., Downs, R. T., Yang, H., and Stone, N. (2016). “1. The power of databases: the RRUFF project,” in *Highlights in mineralogical crystallography* (Berlin, München, Boston: De Gruyter O), 1–30.
- Li, J., Jacobs, A. D., and Hitch, M. (2019). Direct aqueous carbonation on olivine at a CO<sub>2</sub> partial pressure of 6.5 MPa. *Energy* 173, 902–910. doi:10.1016/j.energy.2019.02.125
- Librandi, P., Nielsen, P., Costa, G., Snellings, R., Quaghebeur, M., and Baciocchi, R. (2019). Mechanical and environmental properties of carbonated steel slag compacts as a function of mineralogy and CO<sub>2</sub> uptake. *J. CO<sub>2</sub> Util.* 33, 201–214. doi:10.1016/j.jcou.2019.05.028
- Liu, Z., Lv, C., Wang, F., and Hu, S. (2023). Recent advances in carbonatable binders. *Cem. Concr. Res.* 173, 107286. doi:10.1016/j.cemconres.2023.107286
- Lv, C., Liu, Z., Wang, F., and Hu, S. (2023). Phase evolution and pulverization mechanism of self-pulverizing carbonatable clinkers. *J. Am. Ceram. Soc.* 106 (2), 1391–1412. doi:10.1111/jace.18793
- Mu, Y., Liu, Z., Wang, F., and Huang, X. (2018). Carbonation characteristics of γ-dicalcium silicate for low-carbon building material. *Constr. Build. Mater.* 177, 322–331. doi:10.1016/j.conbuildmat.2018.05.087
- Nielsen, P., Boone, M. A., Horckmans, L., Snellings, R., and Quaghebeur, M. (2020). Accelerated carbonation of steel slag monoliths at low CO<sub>2</sub> pressure – microstructure and strength development. *J. CO<sub>2</sub> Util.* 36, 124–134. doi:10.1016/j.jcou.2019.10.022
- Otsuka, R. (1986). Recent studies on the decomposition of the dolomite group by thermal analysis. *Thermochim. Acta* 100 (1), 69–80. doi:10.1016/0040-6031(86)87051-4
- Patel, A. S., Raudsepp, M. J., Wilson, S., and Harrison, A. L. (2024). Water activity controls the stability of amorphous Ca–Mg- and Mg-carbonates. *Cryst. Growth and Des.* 24 (5), 2000–2013. doi:10.1021/acs.cgd.3c01283
- Peys, A., Pires Martins, N., Prado Araujo, F., Komnitsas, K., and Nielsen, P. (2025). High-temperature slag engineering in pursuit of effective mineral carbonation of pyroxene-rich ferronickel slag. *J. CO<sub>2</sub> Util.* 95, 103077. doi:10.1016/j.jcou.2025.103077
- Peys, A., Van De Sande, J., Teck, P., and Snellings, R. (2021). A metallurgical approach toward bloating of canal-dredging sediments. *J. Sustain. Metallurgy* 7 (4), 1671–1685. doi:10.1007/s40831-021-00441-4
- Sanna, A., Uibu, M., Caramanna, G., Kuusik, R., and Maroto-Valer, M. M. (2014). A review of mineral carbonation technologies to sequester CO<sub>2</sub>. *Chem. Soc. Rev.* 43 (23), 8049–8080. doi:10.1039/c4cs00035h
- Smigelskyte, A., Siaucianus, R., Hilbig, H., Decker, M., Urbonas, L., and Skripkiunas, G. (2020). Carbonated rankinite binder: effect of curing parameters on microstructure, strength development and durability performance. *Sci. Rep.* 10 (1), 14462. doi:10.1038/s41598-020-71270-w
- Snaebjörnsdóttir, S. Ó., Sigfússon, B., Marieni, C., Goldberg, D., Gislason, S. R., and Oelkers, E. H. (2020). Carbon dioxide storage through mineral carbonation. *Nat. Rev. Earth and Environ.* 1 (2), 90–102. doi:10.1038/s43017-019-0011-8
- Stephen Stokreef, F. S., Arthur, S., and Ahmad, G. (2022). Mineral carbonation of ultramafic tailings: a review of reaction mechanisms and kinetics, industry case studies, and modelling. *Clean. Eng. Technol.* 8, 100491. doi:10.1016/j.clet.2022.100491
- Urmos, J., Sharma, S. K., and Mackenzie, F. T. (1991). Characterization of some biogenic carbonates with Raman spectroscopy. *Am. Mineralogist* 76 (3–4), 641–646.
- Valverde, J. M., Perejon, A., Medina, S., and Perez-Maqueda, L. A. (2015). Thermal decomposition of dolomite under CO<sub>2</sub>: insights from TGA and *in situ* XRD analysis. *Phys. Chem. Chem. Phys.* 17 (44), 30162–30176. doi:10.1039/C5CP05596B
- Veetil, S. P., and Hitch, M. (2020). Recent developments and challenges of aqueous mineral carbonation: a review. *Int. J. Environ. Sci. Technol.* 17 (10), 4359–4380. doi:10.1007/s13762-020-02776-z
- Wang, S., Gao, F., Li, B., Liu, Y., Deng, T., Zhang, Y., et al. (2024). Clinkerization of carbonatable belite–melilite clinker using solid waste at low temperature. *Constr. Build. Mater.* 418, 135357. doi:10.1016/j.conbuildmat.2024.135357
- Woodall, C. M., McQueen, N., Pilorgé, H., and Wilcox, J. (2019). Utilization of mineral carbonation products: current state and potential. *Greenh. Gases Sci. Technol.* 9 (6), 1096–1113. doi:10.1002/ghg.1940
- Yadav, S., and Mehra, A. (2021). A review on *ex situ* mineral carbonation. *Environ. Sci. Pollut. Res.* 28 (10), 12202–12231. doi:10.1007/s11356-020-12049-4